PLASTIC DEFORMATION PROCESSES ACCOMPANYING STRESS CORROSION CRACK PROPAGATION IN IRRADIATED AUSTENITIC STEELS[1]

M.N. Gussev[1], G.S. Was [2], J.T. Busby[1], K.J. Leonard[1].

[1] Oak Ridge National Laboratory, One Bethel Valley Road, P.O. Box 2008, MS-6151, Oak Ridge, TN 37831, USA. [2] University of Michigan, 2355 Bonisteel Blvd., Ann Arbor, MI 48109-2104, USA.

Abstract

During stress corrosion crack propagation, stress values in the crack tip vicinity often exceed material yield stress limit. Plastic deformation processes may accompany and influence cracking. Here, stress corrosion crack propagation and deformation mechanisms were investigated using EBSD analysis. The investigated material was 304L Ti-enriched austenitic stainless steel irradiated to 10.4 dpa at 320°C. Crack growth tests were conducted in simulated Normal Water Chemistry (NWC) environment in the temperature range 288-320°C using compact tension specimens. Analyzing crack trajectory and grain structure in the crack vicinity, it was established that grain orientation with respect to the acting stress direction was not a key factor controlling crack propagation. No crystallographic orientation susceptible to cracking was identified. Also, EBSD analysis revealed strong inhomogeneity in plastic strain distribution along the crack path. Most crack-adjacent grains remained virtually strain-free whereas few grains experienced strong plastic strain. These areas were presumed to be “plastic bridges” or “ductile ligaments.”

Keywords: EBSD, stress corrosion cracking, deformation localization, neutron irradiation, austenitic steel.

1. Introduction

Austenitic 300-series steels are widely used in the industry because of their favorable combination of mechanical and corrosion properties and their acceptable radiation tolerance. However, this class of materials suffers from several issues, with the stress corrosion cracking (SCC) susceptibility being one of the most widely recognized problems in the high-temperature operating environments, like Light Water Reactors (LWRs)[1–3]. It is expected that the SCC-related issues will become more severe with the aging of the LWR fleet.

Currently, crack growth rate (CGR) measurements are one of the most common tools for quantifying the material performance and cracking in the corrosion environments. The main outcome of the test is the CGR value as a function of corrosion environment, temperature, stress intensity, and material parameters. A rich literature database exists on the different aspects of SCC propagation mechanisms in non-irradiated materials; however, the role of material structure on crack propagation and plastic deformation mechanisms are still not well understood for materials irradiated at high doses (10 dpa and more). Radiation-induced hardening and the change in the deformation mode from multiple active slip systems to dislocation channeling should influence the advancing crack and the plastic strain fields in the crack-surrounding area. The present work aims to investigate deformation mechanisms and quantify strain fields induced by stress corrosion crack propagation in neutron-irradiated steel.

---

[1] This manuscript has been authored by UT-Battelle, LLC, under Contract No. DE-AC05-00OR22725 with the U.S. Department of Energy. The United States Government retains and the publisher, by accepting the article for publication, acknowledges that the United States Government retains a non-exclusive, paid-up, irrevocable, worldwide license to publish or reproduce the published form of this manuscript, or allow others to do so, for United States Government purposes. The Department of Energy will provide public access to these results of federally sponsored research in accordance with the DOE Public Access Plan (http://energy.gov/downloads/doe-public-access-plan).

2. Experimental procedure

A set of round compact tension (RCT) specimens were produced and irradiated in the framework of the Cooperative Irradiation-Assisted Stress Corrosion Cracking Research (CIR) Program [4,5]. The specimens were irradiated in the BOR-60 fast reactor and tested by several research teams [6–8]. The details on testing history and crack growth results for the specimen studied here (MS-01 RCT specimen, damage dose 10.7 dpa) are given in [9]. The experiment setup is discussed in [10]. The specimen, Figure 1, was pin-loaded and had side groves. The crack growth test was performed under Normal Water Chemistry (NWC) conditions [10], with temperatures varying from 288 to 320°C. Stress intensity factor (K) increased from 16.28 MPa × $m^{0.5}$ at the beginning of the test to the value of 29.33 MPa × $m^{0.5}$ at the test end.

For investigation of the microstructural influence on crack behavior, the post-tested RCT sample was sectioned in half to reduce the activity level; the rounded bottom part with the pin hole was removed. Details are shown in Figure 2. The remaining slice with ~2.5 mm thickness was cut once again to produce cross-sectional slices. The cross section plane location is identified in the figure; it was important to capture the maximal portion of the stress corrosion crack. The cross-section was located close to the middle plane of the RCT specimen and represented, as believed, the plane strain state. The cross-sectional sample was prepared by mechanical grinding and polishing. The last mechanical polishing step was 0.5 μm sandpaper to keep the sharp and non-damaged edges. The final preparation step was electropolishing in a Struer A2 solution for 2 seconds (nominally 15 to 60 s would be used) to keep the sample edges as sharp as possible. Attempts at electropolishing for 5 to 10 s produced slightly rounded edges destroying the crack-adjacent layer of grain. It was believed for the given material under the given electropolishing conditions (2 sec at 30 V DC), ~ 3 μm of material was removed near the crack edge.

EBSD analysis was performed on a VERSA 3D FEG scanning electron microscope. The operational voltage was 20 kV. A rectangular grid was used; step size varied from 1-2 μm for general structure scan to 125 nm for high-resolution scans in the crack-adjacent area. To characterize plastic strain distribution, several EBSD strain metrics were used: (1) Kernel Average Misorientation or KAM, (2) Grain Reference Orientation Deviation or GROD, and (3) Grain Average Misorientation or GAM. These metrics are widely described and analyzed in the literature [11–13]. Unless otherwise stated, all KAM, GROD, and KAM values discussed below in the text were calculated for the step size of 125 nm.

3. Experimental results and their discussion

After sample preparation, several EBSD scans were performed at a depth of ~1.5–1.7 mm from the fracture surface, below the SCC and other deformed areas, to analyze the material structure and phase composition. Figure 3 shows typical EBSD data for the bulk material. The irradiated material had relatively small average grain size, about 10 μm, and a pronounced bimodal grain size distribution. Small grains formed specific clusters and bands, and large grains often grouped together. Whereas the bimodal grain distribution was observed for all analyzed areas, the fraction and the average size of large grains varied slightly across the structure suggesting some minor structure inhomogeneity.

Two phases were identified: (1) austenite, face-centered-cubic, and (2) delta-ferrite, body-centered-cubic. The amount of delta-ferrite visible with EBSD was estimated to be ~1–1.5%. Ferrite grains formed groups and colonies; the ferrite grains often had larger KAM values compared to the surrounding austenite grains. No visible texturing was observed. The bulk structure was found to consistent with an annealed structure; no specific signs of pre- or post-irradiation cold work was observed using EBSD. Expected values GROD, a common EBSD strain metric providing a measure of local in-grain misorientation, for strain free grains are between 0.1–0.2°. Average GAM parameter for the non-deformed material was ~0.13-0.15°. Average KAM value for austenite was ~0.13-0.17°; ferrite grains in bulk often had slightly higher values and were excluded from analysis.

Figure 4 shows an example of the EBSD data set collected along the crack propagation path. The scan was performed at a magnification of 1000× with 125 nm step (pitch). The separate scans taken along the crack path, overlapped at ~20–30 μm, allowing for stitching. The depth (distance from the crack edge) varied slightly for different scans from ~30-40 to 50–70 μm depending on the local crack trajectory. As expected, such depth should reveal plastic strain in the crack-adjacent layer and show strain gradients.

It is important to underline that, although the scan location was known, it was very difficult, if possible at all, to connect the collected EBSD data to the particular stress intensity factor value or other parameters during the CGR test [9]. The CGR testing provides an average crack length value [7,10] whereas crack front often had curved or complex shape (Figure 2), so only rough K-value may be estimated.

From the EBSD results, the crack-adjacent grains often have some signs of plastic strain; for the GROD map in Figure 4, plastic strain is visible as a smooth change in color from blue to green and yellow. The width of the crack-adjacent area with signs of plastic strain is ~10-15 μm, and is slightly more in some cases. GROD value for the crack-adjacent grains may reach ~10° for some grains.

An important feature in Figure 4 is the absence or very low level of misorientation in many crack-adjacent grains. Instead of high strain level in the neighboring grains, significant grain fraction practically zero misorientation variations. Deformed and non-deformed grains interlaced along the crack path pointing on the strong plastic strain inhomogeneity.

Figure 5 shows an additional EBSD data set with one specific feature. Many grains in the GROD map are strain free (blue color); however, grains in the image center show pronounced local misorientation. The deformed grains are grouped together, contrasting with the neighboring weakly or non-deformed area. These highly deformed areas, termed below as "deformation hot spots", occupied ~10–15% of the overall analyzed crack path.

Figure 6 show the hot spot from Figure **5** in more detail providing GAM and KAM maps. One may see visible striations in KAM and GAM color codes images representing higher deformation values at this particular location, the depth of these features extending ~ 15-25 μm. These features suggest the presence of pronounced slip lines or dislocation channels. Dislocation channels (slip bands), as a rule, are not expected to appear in the image quality (IQ) maps. However, for this particular location, Figure 6, some darker contrasting feature are visible in the IQ maps that correlate to the KAM and GROD maps. Grain boundary network map (overlayed on the IQ map of Figure 6) also demonstrated several small grains separated by low-angle boundaries. One may argue these subgrains formed during cracking.

Figure 7 shows another unique region containing a small (~20–25 μm) secondary crack. Here, the IQ map shows some widening of the secondary crack away from the main crack; the lost of the crack edge material due to specimen preparation (electropolishing) may be estimated as ~2-3 μm or less for each crack side. Additionally, one may see that electropolishing induced rounding of the crack edges making the analysis of the crack surface oxidation unobtainable.

By analogy with the above-discussed results, one may see strong inhomogeneity of plastic strain in GROD and KAM maps, Figure 7; many grains were strain free whereas others experienced pronounced plastic strain. Plastic strain quantification by the GAM parameter demonstrated that many grains are practically strain-free, with GAM < 0.2°, which is close to the bulk value. These results suggest crack may propagate via the structure at stresses significantly lower than the material yield stress. In some cases, the crack tip movement through the structure did not induce plastic strain in many crack-adjacent grains.

To measure the thickness of the plastically deformed layer and quantify plastic deformation, a detailed analysis of the KAM profiles was conducted. To reduce local fluctuation role and noise level, the KAM values were averaged for 10 pixels located at the same depth, and the profile was calculated in the normal direction relative to the fracture surface. Figure 8 shows several KAM profiles for the most typical areas.

Profiles #1 and #2 intersect several strain-induced features at small depths (<5 μm), which look like low-angle (<5°) in-grain boundary (LAB). LABs provide a small local increase in KAM (from ~0.15-0.18°, i.e., bulk level, to ~0.4–0.5°). Below ~5 μm the material appeared to be unstrained, and the KAM profile curves (#1 and #2) were close to the bulk values (~0.18°). Interestingly, LABs often presented in the austenitic grains near the crack edge. These structure elements (LAB) might be seen as a sharp local increase in KAM, and often were also visible in the IQ maps. The LABs were much rarer in bulk, far from the crack edge.

Profiles #3 and #5 were taken in the grains without visible plastic strain. Indeed, regardless of the depth, the KAM value remained around bulk values (~0.18°). It appears that material at these locations did not reveal plastic strains even in the crack vicinity. The local fluctuation in profile #3 at 10–15 μm of depth was caused by a scratch. Profile #4 had few maximums, related to both cracking and scratches. The first maximum, at the crack edge, was most likely induced by plastic strain. The second, at ~5–6 μm depth, corresponded to the LAB and the last one, at ~13 μm depth was caused by surface scratching. Thus, as follows from the KAM profiles, most plastic strain, if it appeared during crack propagation, was localized in the ~5–10 μm layers. The strain tended to be localized to some grains, whereas other grains near the crack edge remained un-deformed.

The complex character of strain localization required further analysis to explain the appearance of multiple strain-free grains. Grain orientation to the acting stress strongly influences the elastic and plastic behavior of the grain (Schmid and Taylor factors). If crack propagation depends on the stress field near the crack tip, and on the grain Schmid factor, grain population in the crack-adjacent area may be different than that of the bulk. Figure 9 shows this comparison between the crack-adjacent grains and that of the bulk material. The number of data points was limited (only two scans were included in the figure) to keep the image readable. As follows from the plot, there is no pronounced difference between cracked and non-cracked grain populations. At least, this difference was weak and did not lead to the pronounced depopulation of any unit triangle area.

To analyze the grain orientation role in more detail, a series of EBSD scans (>250 crack-adjacent grains) were merged, and the orientation of the crack-adjacent grains was compared to the summary data for the grains farther from the crack (Figure 10). As shown in the texture plots, the general texturing in the bulk material, far from crack, was weak enough, only ~1.53 × random. The most pronounced texturing component was an increased fraction of [001]-oriented grains in the crack propagation direction (A-group), [010] in Figure 10. Two other specific areas (B, C) were just slightly above the average (~1.1 and ~1.2 × random, respectively).

Comparing the grain orientation patterns in bulk and near the crack, one may see that crack-adjacent grain orientations are, in general, close to the non-cracked ones. Grains with [001]-orientation with respect to the crack propagation direction (group marked as “A” in Figure 10) have a texture index of ~1.5 × random in bulk and ~1.6 × random near the crack. Two other specific areas (B and C) have similar texture indexes (B: ~1.1 × random in bulk and ~1.5 × random after cracking; C: ~1.2 ×random in bulk and ~1.6 × random after cracking). Some weak secondary effects may be present; however, they appear to be insignificant.

At the moment, it is possible to conclude that grain orientation plays a weak, if any, role on the stress corrosion cracks advancing. No one grain population (e.g., grains with [111] or [001] orientation) dominated along the crack path.

Conclusions

In the present work, the stress corrosion crack propagation was investigated in detail for a highly-irradiated (10.4 dpa) austenitic steel specimen. Using SEM-EBSD approach, plastic stain fields and deformation localization were analyzed in a neutron-irradiated round compact tension specimen of model

304 steel tested under NWC conditions. No pronounced crack branching was observed; only a few short, less than 40–50 μm secondary cracks were found in the structure.

EBSD analysis revealed strong inhomogeneity in plastic strain distribution along the crack path. Some crack-adjacent grains remained virtually strain-free whereas few grains experienced strong plastic strain. These areas were presumed to be "plastic bridges" or "ductile ligaments." The width of the plastically deformed areas along the crack was, in most cases, 5–10 μm or less; this value increased up to ~20–50 μm inside the plastic bridges.

Grain orientation with respect to the acting stress direction was not a major factor controlling crack propagation. No crystallography orientation susceptible to crack propagation was identified by this work.

References

[1] K. Fukuya, "Current understanding of radiation-induced degradation in light water reactor structural materials," *Journal of Nuclear Science and Technology*, vol. 50, 2013, pp. 213–254.

[2] Z. Jiao and G. Was, "Impact of localized deformation on IASCC in austenitic stainless steels," *Journal of Nuclear Materials*, vol. 408, 2011, pp. 246–256.

[3] G.S. Was, Y. Ashida, and P.L. Andresen, "Irradiation-assisted stress corrosion cracking," *Corrosion Reviews*, vol. 29, 2011, pp. 7–49.

[4] J. Massoud, P. Dubuisson, P. Scott, and V. Chamardine, "CIR II program: description of the Boris 6 and 7 experiments in the BOR-60 fast breeder reactor," *EPRI Report*, vol. 1011787, 2005.

[5] P. Scott, "Materials reliability program: a review of the cooperative irradiation assisted stress corrosion cracking research program (MRP-98)," *EPRI Report*, vol. 1002807, 2003.

[6] M. Ernestova and J. Burda, "Crack growth testing of tailored alloys from Boris 6 and 7 irradiations," *EPRI Report*, vol. 1021235, 2009.

[7] A. Jenssen, J. Stjärnsäter, and R. Pathania, "Crack growth rates of irradiated commercial stainless steels in BWR and PWR environments," *15th International Conference on Environmental Degradation of Materials in Nuclear Power Systems-Water Reactors*, Wiley Online Library, 2011, pp. 1229–1240.

[8] S. Van Dyck, "IASCC mechanisms-controlling material factors: SCC crack-growth tests on selected Boris-6 tailored heats," *Palo Brussels, Belgium: SCK-CEN*, 2009.

[9] G.S. Was, Y. Ashida, K.J. Stephenson, A. Flick, and P.L. Andersen, "Identifying Mechanisms and Mitigation Strategies for Irradiation Assisted Stress Corrosion Cracking of Austenitic Steels in LWR Core Components," *EPRI Report*, vol. 3002003105, 2014.

[10] Y. Ashida, A. Flick, P.L. Andresen, and G.S. Was, "The Key Factors Affecting Crack Growth Behavior of Neutron-Irradiated Austenitic Alloys," *15th International Conference on Environmental Degradation of Materials in Nuclear Power Systems-Water Reactors*, Wiley Online Library, 2011, pp. 1241–1254.

[11] masayuki Kamaya, K. Kubushiro, Y. Sakakibara, S. Suzuki, H. Morita, Y. Rika, D. Kobayashi, K. Yamagiwa, T. Nishioka, Y. Yamazaki, and others, "Round robin crystal orientation measurement using EBSD for damage assessment," *Mechanical Engineering Journal*, vol. 3, 2016, pp. 16–77.

[12] S. Wroski, J. Tarasiuk, B. Bacroix, A. Baczmaski, and C. Braham, "Investigation of plastic deformation heterogeneities in duplex steel by EBSD," *Materials Characterization*, vol. 73, 2012, pp. 52–60.

[13] R. Yoda, T. Yokomaku, and N. Tsuji, "Plastic deformation and creep damage evaluations of type 316 austenitic stainless steels by EBSD," *Materials characterization*, vol. 61, 2010, pp. 913–922.

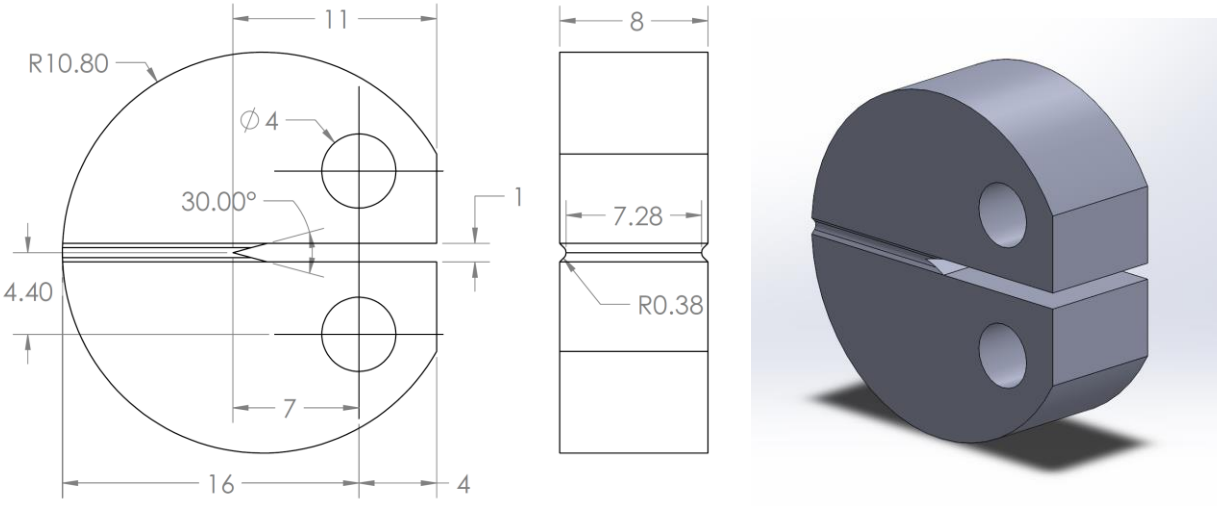

Figure 1. Dimensions and the shape of the RCT specimen.

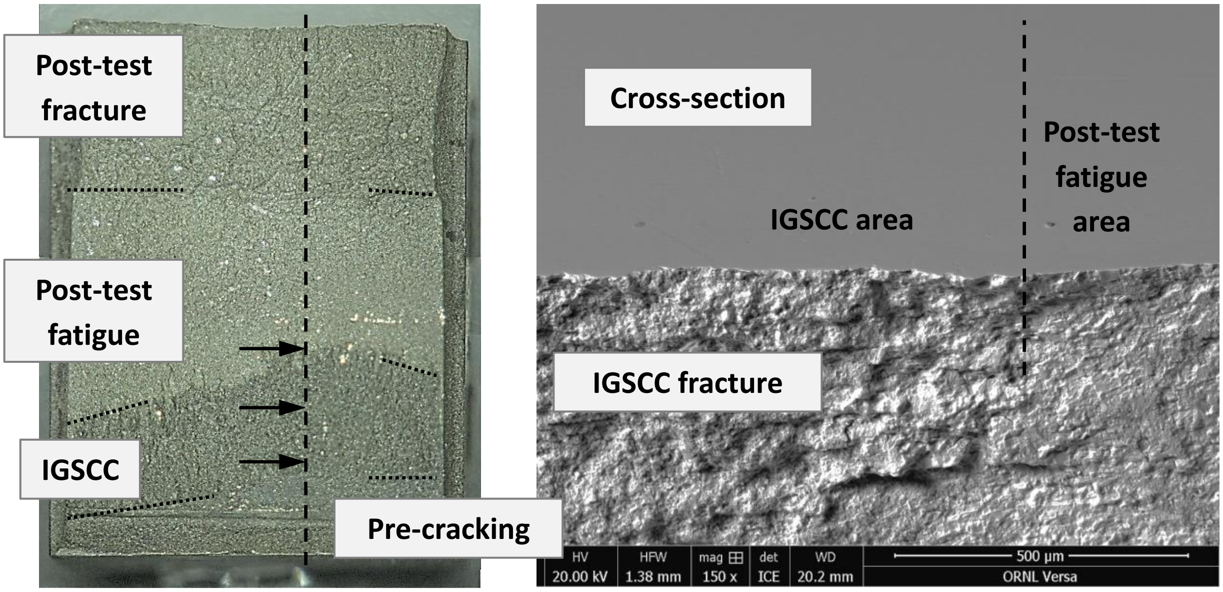

Figure 2. Left: Specimen surface showing different fracture mechanisms (Pre-cracking, Inter-granular stress corrosion cracking, etc.); dashed line and black arrow show the location of the prepared cross-section. Right: a tilted view of the specimen cross-section prepared for EBSD analysis; one may see the transition between IGSCC area and post-test fatigue.

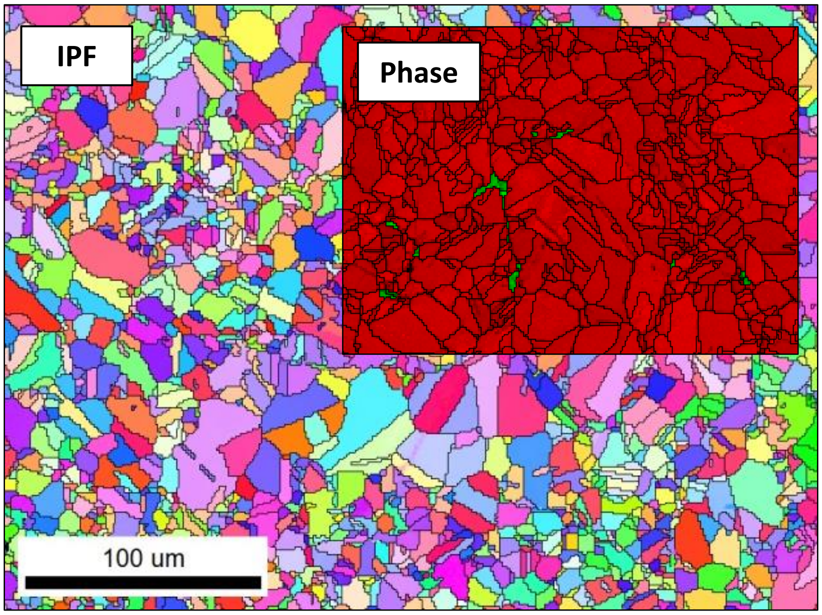

Figure 3. EBSD IPF map showing grain morphology for the investigated material. Insertion demonstrates the Phase map for the same area (austenite is red, delta-ferrite is green).

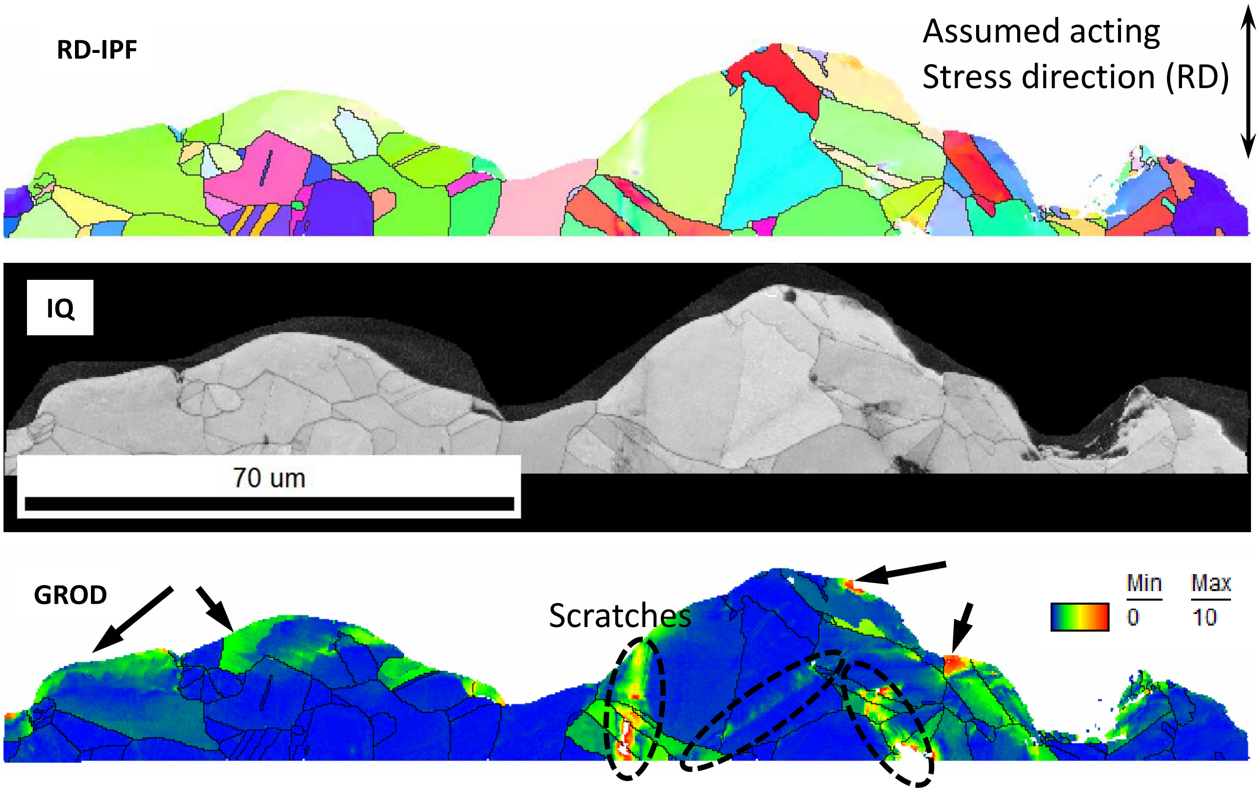

Figure 4. Typical EBSD dataset for the crack-adjacent area: IPF (Inverse Pole Figure), colored in the RD (acting stress) direction, IQ (Image Quality), and GROD (Grain Reference Misorientation Deviation) maps. Black arrows mark locations with high local strain level; dashed ovals show scratches introduced during specimen preparation.

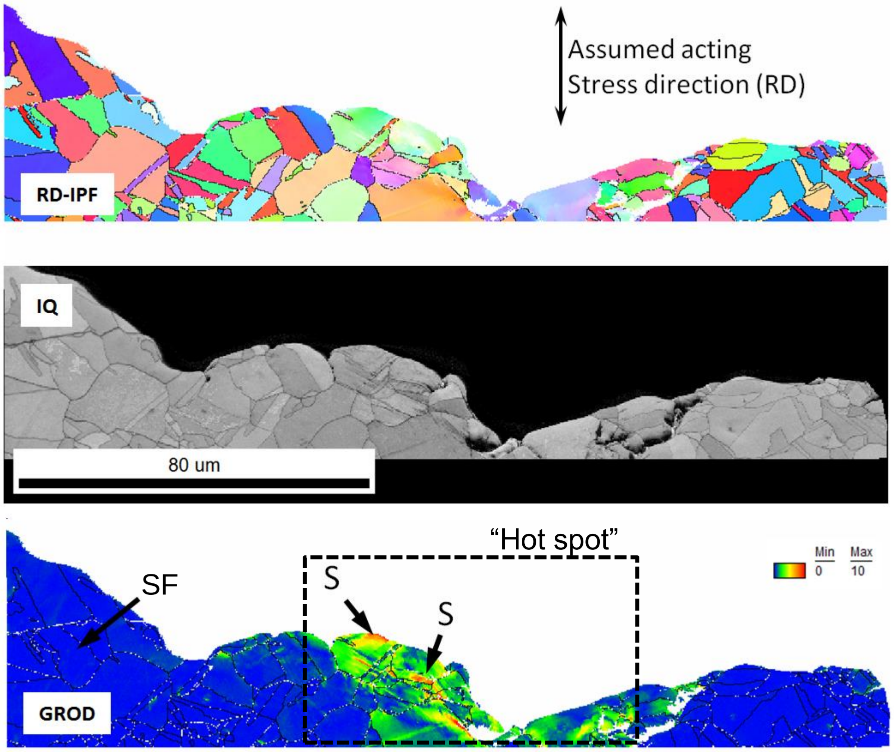

Figure **5**. EBSD data for the crack-adjacent area showing a spot with high local strain level. S: areas with high local misorientation (GROD). The GROD scale here was limited by 10°.

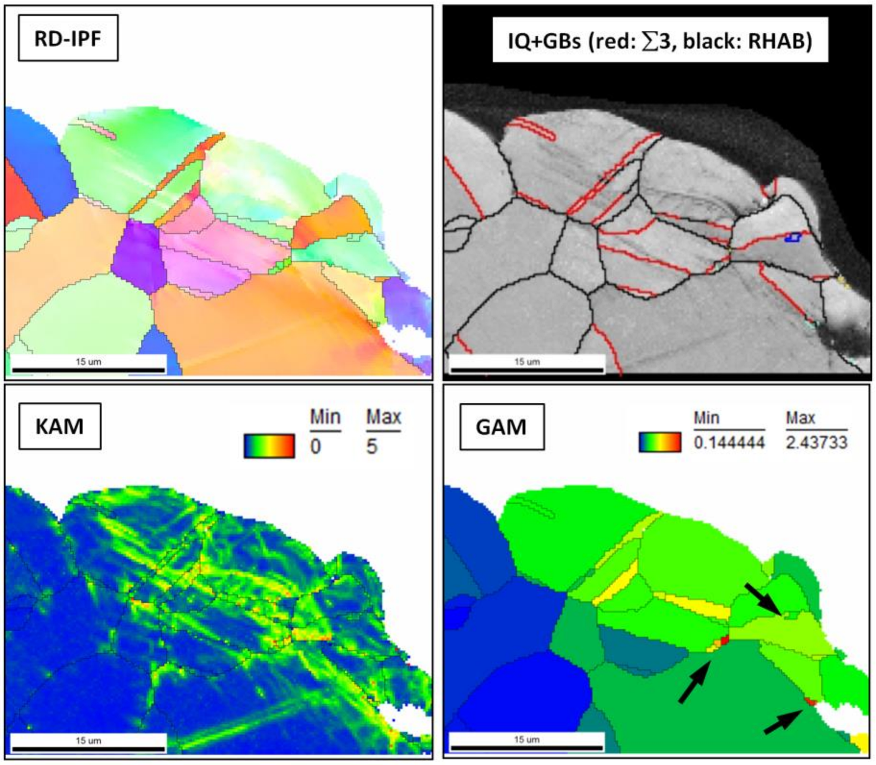

Figure 6. EBSD data set for the highly-strained area (deformation “hot spot”). Black arrows point small grains, as believed, formed because of plastic deformation.

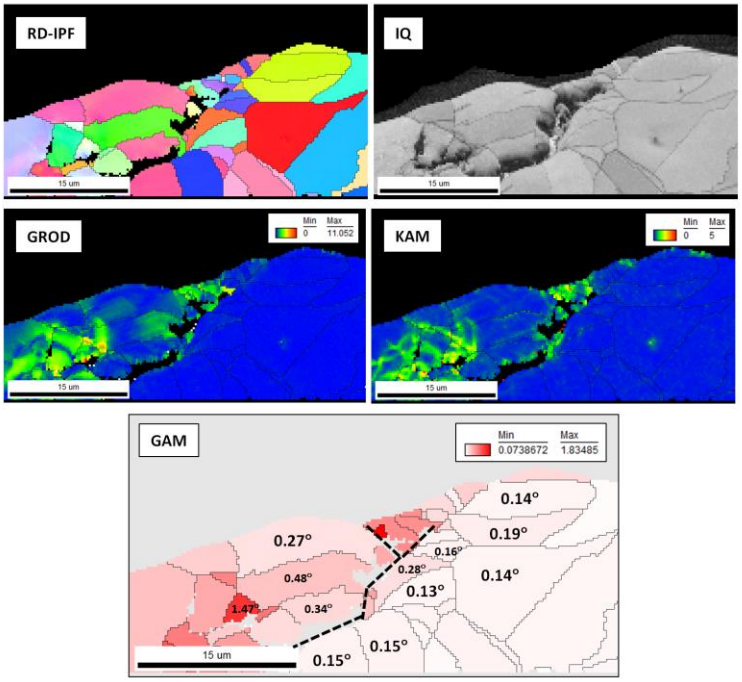

Figure 7. EBSD dataset for the area with small secondary crack (dashed black line). Step size 125 nm. The map shows the GAM value for some crack-adjacent grains.

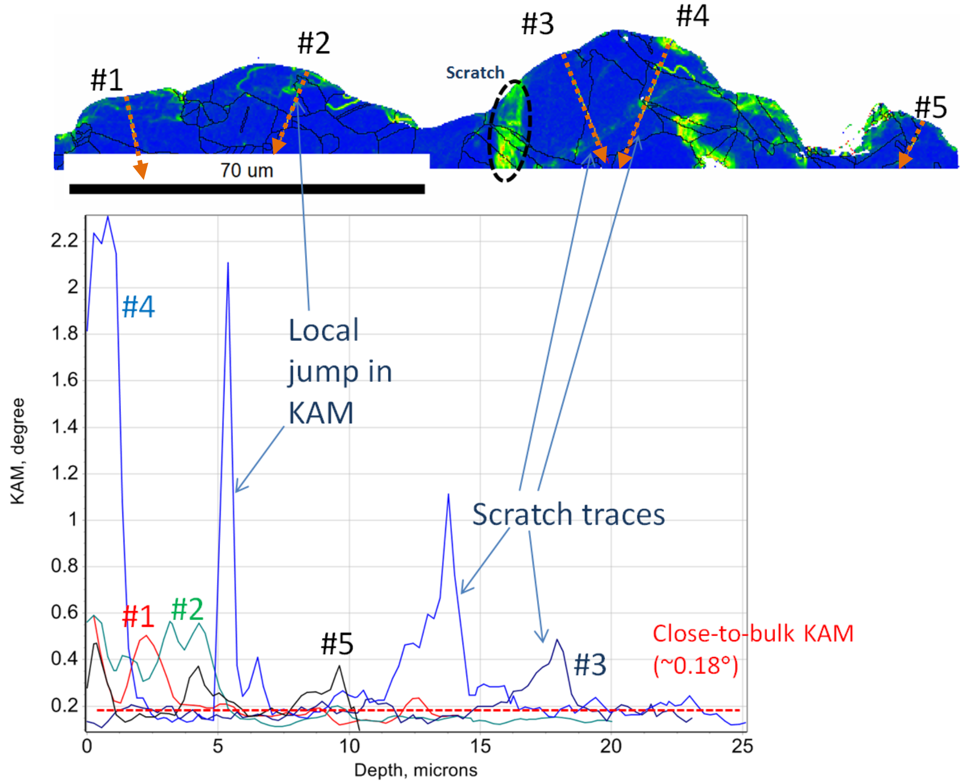

Figure **8**. KAM profiles (#1–5) for the EBSD scan shown in Figure 4. The average width of 10 data points.

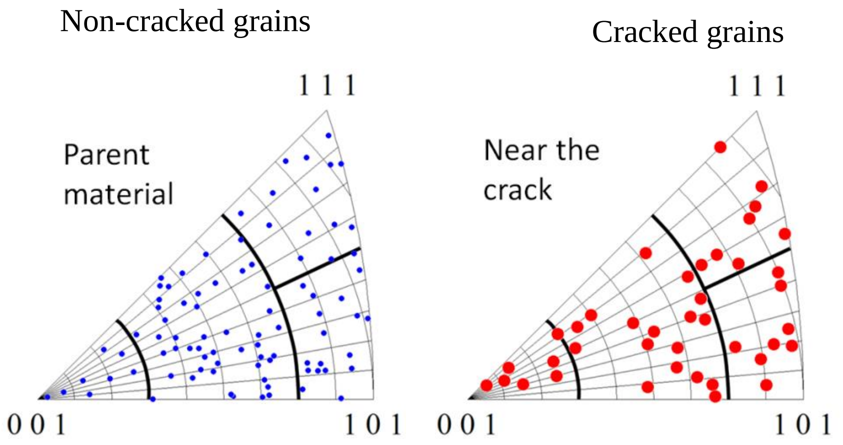

Figure 9. The orientation of crack-adjacent grains compared to randomly selected grains in bulk. The IPFs are plotted with respect to the acting stress during the crack growth test.

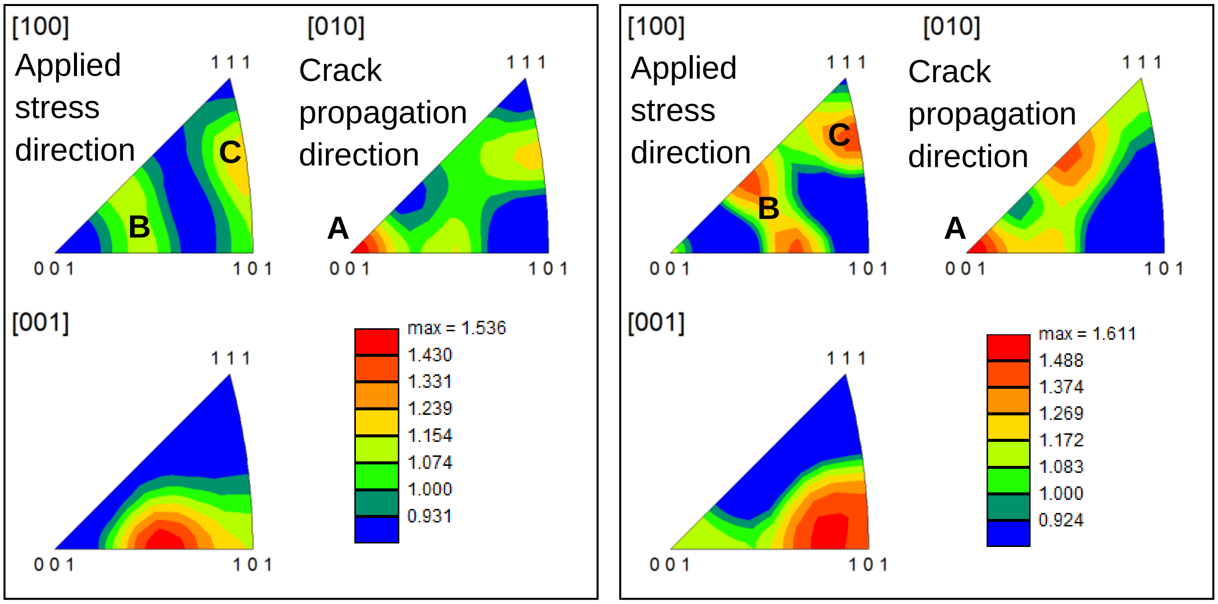

Figure 10. The texture in the bulk non-cracked material (left) and summary texture plot for the crack adjacent grains. The summary plot for 8 scans (same step size and imaging conditions).